A semi-microscopic self-consistent mean-field study of α-decay fine structure of odd-N isotopes along $^{295-303}$120 chains

W. M. Seif[1,2,3†] A. Nasr[1‡]

[1]Cairo University, Faculty of Science, Department of Physics, Giza 12613, Egypt
[2]Joint Institute for Nuclear Research, Dubna 141980, Russia
[3]The Academy of Scientific Research and Technology, Cairo 4262104, Egypt

Abstract: We performed axially deformed HFB calculations with the Skyrme-SLy4 energy density functional (EDF) for isotopes in the even-odd $^{295-303}$120 α-decay chains to study their single-particle structure, deformations, and α-decay fine-structure patterns. Ground and excited states were generated by blocking the corresponding quasineutron configurations. The α-decay half-lives were computed consistently within the preformed cluster model employed, using a nucleus-nucleus potential derived from the same EDF and the WKB approximation. The evolution of single-neutron states proceeds sequentially under prolate deformation from $1/2^+[620]$ and $3/2^+[622]$ states above $N = 152$, through $9/2^+[615]$ and $11/2^-[725]$, to $3/2^+[611]$ for $N = 163 - 167$, and then to $1/2^+[611]$ followed by $9/2^+[604]$ as the prolate deformation decreases toward $N = 169 - 171$. A pivotal shift to oblate deformation occurs around $N = 175$, favoring the $1/2^+[640]$, $3/2^+[642]$, and $5/2^+[642]$ sequence, followed by $1/2^+[620]$ and later alternating states such as $3/2^+[651]$ and $1/2^+[660]$, as the oblate deformation decreases. Approaching $N = 184$, the ground state stabilizes in the spherical $1/2^+[600]3d_{3/2^+}$ orbital. In addition to the predicted rich decay schemes for ^{291}Og, ^{283}Fl, ^{281}Cn, and ^{275}Sg, branching ratios above 55% for α-decay through excited states are indicated for ^{295}120, ^{297,299}Og, ^{287,293}Lv, and ^{283}Fl. The estimated half-lives range from ms (^{301,303}120, ^{289}Lv) and fractions of a second (^{297,299}Og) to hundreds of seconds (^{291}Fl, ^{287}Cn, ^{273,275}Sg), with long ^{295,297,299}120 decay chains extending to Rf.

Keywords: fine structure, α-decay, super-heavy nuclei, HFB calculations, half-life, branching ratio

DOI: 10.1088/1674-1137/ae8ce6 **CSTR:** 32044.14.ChinesePhysicsC.50104110

I. INTRODUCTION

Fine-structure investigations of α-decay chains are a fundamental tool for exploring the superheavy region, providing critical insights into nuclear structure, stability, and the limits of the nuclear chart. Specifically, detailed spectroscopy of decays yields essential data on decay energies, half-lives, and branching ratios. Such information reveals underlying nuclear properties such as deformation, shell effects, single-particle configurations, and shape coexistence that may stabilize nuclei near the predicted "island of stability". By deducing the level schemes of parent and daughter nuclei, these studies validate and refine theoretical models, guide the identification of newly synthesized isotopes, and enable more accurate predictions of decay properties. This, in turn, is crucial for planning future experiments aimed at producing heavier elements. In particular, studying α-decay in odd-N superheavy nuclei (SHN) provides unique insights beyond even-N systems. The unpaired neutron enables detailed probes of single-particle structure, revealing specific orbitals, spin-parity assignments, and decay hindrances. Furthermore, these studies illuminate the competition between decay modes and are crucial for refining nuclear models by testing predictions for pairing, blocking, and shell effects near the Fermi surface.

The atomic nucleus is not a rigid or static system, but instead exhibits collective motion governed by a balance of potentials. The liquid-drop model (LDM) provided an early macroscopic description of this collective behavior, successfully capturing key features of fission and the overall trends in binding energy [1], without explaining magic numbers and nuclear deformations. A complete understanding of nuclear structure emerged from modeling the nucleus as a self-adaptive system, in which a self-consistent mean field links microscopic interactions and macroscopic shape [2−4]. Consequently, key properties such as deformation and decay are governed by the potential energy surface (PES). Macroscopic models provide a smooth PES that successfully describes the sta-

Received 2 June 2026; Accepted 16 July 2026; Accepted manuscript online 17 July 2026

† E-mail: wseif@sci.cu.edu.eg
‡ E-mail: anasr@sci.cu.edu.eg

bility of heavy nuclei but fails for SHN, isomerism, and shape coexistence [5, 6]. The key breakthrough came from the microscopic view in terms of the deformed shell model [7, 8], which successfully explains these phenomena, including magic numbers and the stability of SHN. Modern calculations of PES rely on either macroscopic-microscopic (MM) or fully microscopic frameworks. The MM method combines a liquid-drop or energy density functional (EDF) baseline with Strutinsky shell and BCS pairing corrections [9−11]. In parallel, fully microscopic models use self-consistent Hartree-Fock or Hartree-Fock-Bogoliubov (HFB) theories with semi-realistic or realistic effective interactions to provide a detailed, unified description of nuclear structure from ground states to excited and isomeric states of SHN [2, 12, 13].

Although ground-state to ground-state decays are well characterized, they are less informative than decays involving excited states, which provide a richer array of structural information [14−16]. Beyond γ-ray emission, α-decay spectroscopy serves as a probe of shell structure and collective excitations in parent and daughter nuclei, and is a key indicator of single-particle structure [17−22]. Other processes such as β-decay, cluster radioactivity, and both spontaneous and induced fission [23], along with their respective spectroscopy, further contribute to a comprehensive understanding of nuclear structure [24, 25]. Advanced high-precision spectroscopic techniques facilitate comprehensive mapping of nuclear energy levels [26]. A crucial scientific advance is the mapping of decay chains, which reveal the stepwise transformation of one radioactive element into another through successive decays [25, 27]. This is instrumental in gaining insight into nucleosynthesis and the elemental abundances in the universe [28], and it provides a unique window into the structure of SHN, which are challenging to detect directly [11, 25, 29, 30].

Continuing our earlier investigation of the even-even decay chains ($^{296-304}$120)reported in Ref. [31], we now turn to the more complex and information-rich odd-neutron isotopes of $Z = 120$, with mass numbers from 295 to 303, which lie just below the $N = 184$ neutron shell closure. Unlike even-even systems, in which single-particle spectroscopic information is inaccessible, this work addresses a different problem involving quasiparticle blocking, spin-parity evolution, and fine-structure decay patterns. Odd-neutron nuclei offer opportunities to investigate single-particle structure, pairing correlations, and the influence of the unpaired neutron on the pairing field, as well as the deformation evolution from prolate to oblate to spherical configurations as N approaches 184. These features allow the evolution of level density and the emergence of shell gaps to be examined. The self-consistent mean-field solutions and spectroscopic predictions obtained here complement those obtained in our earlier even-even analysis. We employ the same theoretical framework that combines the HFB and Preformed Cluster Models (PCM). Crucially, both models are based on the same Skyrme-SLy4 EDF and its associated nucleus-nucleus potential, ensuring a consistent description of the single-particle structure, branching ratios, and decay characteristics.

The paper is organized as follows. Section II outlines the theoretical framework, specifically the HFB method used for structural calculations and the PCM and nucleus-nucleus models employed for α-decay. The subsequent Section III presents the results of our investigation into neutron single-particle level ordering beyond the $N = 152$ gap, extending to $N = 184$, and its correlation with the evolving prolate and oblate quadrupole deformation along the ($^{295-303}$120) even-odd decay chains, employing blocked quasiparticle configurations. Explicit calculations of 136 decay modes to ground and low-lying states are presented, revealing longer decay chains than in the even-even cases. The work concludes with a summary of the key findings in Section IV.

II. THEORETICAL FRAMEWORK

This study uses the mean-field HFB method to describe nuclear structure microscopically by including both particle-hole and particle-particle correlations self-consistently. We solve the HFB equations with the HFBTHO code [32−35], which assumes axial and reflection symmetries. Compared with earlier versions, the HFBTHO (v4.0) code [32] used here provides a more accurate treatment of broken symmetries, including time-reversal symmetry, thereby improving the description of odd-even nuclear structure. We use the SLy4 parameterization [36] of the Skyrme EDF because of its proven accuracy in modeling nuclear structure, decay, and reactions. The resulting binding energy, deformation, and single-particle spectra are used in the α-decay calculations based on the preformed cluster model (PCM) [37, 38], using the α-daughter potential obtained from the same SLy4 EDF.

To describe atomic nuclei, the HFB method provides a unified framework that captures both the average mean-field influence on each particle and the tendency of particles to form bound pairs [2, 12, 39, 40] by redefining the system's ground state as a "quasiparticle vacuum". These quasiparticles are not fundamental particles but emergent hybrids, formed as superpositions of particles and holes through a mathematical Bogoliubov transformation in terms of single-particle creation and annihilation operators, starting from the second-quantized many-body Hamiltonian

$$\hat{H} = \sum_{mn} e_{mn} c_m^{\dagger} c_n + \frac{1}{4} \sum_{mnpq} \bar{v}_{mnpq} c_m^{\dagger} c_n^{\dagger} c_q c_p \,. \tag{1}$$

Here, $c_m^\dagger$ (c_n) creates (annihilates) a nucleon in a single-particle state m (n), e_{mn} are kinetic-energy matrix elements that may include a one-body potential, and $\bar{v}_{mnpq}$ are the matrix elements of the antisymmetrized two-body interaction, $\bar{v}_{mnpq} = \langle mn|V|pq\rangle - \langle mn|V|qp\rangle$, where V denotes the effective nucleon-nucleon (NN) interaction. Antisymmetrization explicitly enforces the Pauli exclusion principle. The Bogoliubov transformation reads

$$\begin{pmatrix} \alpha^\dagger \\ \alpha \end{pmatrix} = \begin{pmatrix} U^\dagger & V^\dagger \\ V^T & U^T \end{pmatrix} \begin{pmatrix} c^\dagger \\ c \end{pmatrix}, \tag{2}$$

which is equivalent to $\alpha_k = \sum_n U_{nk}^* c_n + V_{nk}^* c_n^\dagger$ and $\alpha_k^\dagger = \sum_n U_{nk} c_n^\dagger + V_{nk} c_n$, where U and V are matrices that transform single-particle states into quasiparticle states. $\alpha_k^\dagger$ (α_k) create (annihilate) quasiparticles.

To derive the HFB equations, one performs a constrained minimization of the system's energy to ensure that the generalized density matrix R satisfies the required idempotency property. Through R, the theory naturally combines the normal mean-field interactions, represented by the normal density matrix $\rho = V^* V^T$, with the pairing correlations, represented by the pairing tensor $\kappa = V^* U^T$. The quasiparticle vacuum $|\Phi\rangle$, defined by $\alpha_k|\Phi\rangle = 0$ for all k, serves as the HFB ground state, for which the one-body density matrix ρ and the pairing tensor κ are given by

$$\begin{aligned} \rho_{nn'} &= \langle\Phi|c_{n'}^\dagger c_n|\Phi\rangle = (V^* V^T)_{nn'}, \\ \kappa_{nn'} &= \langle\Phi|c_{n'} c_n|\Phi\rangle = (V^* U^T)_{nn'}. \end{aligned} \tag{3}$$

The energy of the HFB ground state is obtained via the variational principle with respect to ρ and κ, subject to particle-number conservation enforced by Lagrange multipliers, which yields the HFB equations in the form of a generalized eigenvalue problem,

$$\begin{pmatrix} h-\lambda & \Delta \\ -\Delta^* & -h^*+\lambda \end{pmatrix} \begin{pmatrix} U_k \\ V_k \end{pmatrix} = E_k \begin{pmatrix} U_k \\ V_k \end{pmatrix}. \tag{4}$$

Here, h denotes the Hartree-Fock single-particle Hamiltonian, λ is the chemical potential enforcing the correct average particle number, Δ is the pairing-field potential, $E_k \geq 0$ are quasiparticle energies, and U_k and V_k are the quasiparticle wave-function components. By iteratively updating h and λ from the computed densities, this self-consistent framework efficiently describes the nuclear shape, pairing, and ground-state properties upon convergence.

EDF provides a framework for implementing the HFB formalism [12, 40, 41], in which the total energy is expressed as a functional of the local densities, $E[\rho,\kappa] = \int \mathcal{H}(\boldsymbol{r})\mathrm{d}^3 r$, with $\mathcal{H}(\boldsymbol{r}) = \mathcal{H}_0(\boldsymbol{r}) + \mathcal{H}_{\rm pair}(\boldsymbol{r})$ representing the sum of the mean-field ($\mathcal{H}_0$) and pairing ($\mathcal{H}_{\rm pair}$) energy densities. The relevant proton ($q = p$) and neutron ($q = n$) densities include the standard particle, kinetic, and pairing densities, as well as the spin-orbit current $\boldsymbol{J}_q$ and current density $\boldsymbol{j}_q$ contributions. These densities are derived from the single-particle wave functions $\phi_{kq}(\boldsymbol{r})$ for each state, their corresponding occupation probabilities v_k^2, and the Pauli spin matrices $\hat{\boldsymbol{\sigma}}$. For even–even nuclei with time-reversal symmetry, the current density j_q vanishes in the ground state. Because they break time-reversal symmetry, blocked configurations in odd-A nuclei require time-odd densities, which are also vital for collective dynamics [41]. By expanding quasiparticle wave functions in a cylindrical transformed harmonic oscillator basis, the HFB equations are solved without explicitly discretizing space. However, local densities such as the particle, kinetic-energy, and spin-current densities can be explicitly calculated on a two-dimensional (r,z) grid during the iterative solution, since the energy density functional is an integral of these local fields over coordinate space. Through this reconstruction, the radial density $\rho(r)$ is extracted directly for spherical nuclei, or after angular averaging for deformed ones, thereby providing the spatial dependence of the mean-field potential and energy functional as functions of r.

The mean-field EDF is composed of kinetic, nuclear ($\mathcal{H}_{Sky}$), and Coulomb ($\mathcal{H}_C$) contributions [36],

$$\begin{aligned} \mathcal{H}(\boldsymbol{r};\rho_i,\tau_i,J_i) =& \frac{\hbar^2}{2m}\sum_{i=p,n}\tau_i(\boldsymbol{r};\rho_i) + \mathcal{H}_{Sky}(\boldsymbol{r};\rho_i,\tau_i,J_i) \\ &+ \mathcal{H}_C(\boldsymbol{r};\rho_p). \end{aligned} \tag{5}$$

The central part ($\mathcal{H}_{Sky}$) of the Skyrme EDF describes the effective NN interaction in terms of zero- and finite-range, effective-mass, momentum- and density-dependent, and spin-orbit contributions, as well as a nonlocal spin-gradient tensor coupling. Further details on the standard formalism of the Skyrme EDF and its SLy4 parameterization, which is used here, are provided in Refs. [36, 42, 43]. The Coulomb contribution, arising from the proton-proton electrostatic interaction, consists of a direct (Hartree) part and an exchange (Fock) term, described using the Slater approximation,

$$\mathcal{H}_C = \frac{e^2}{2}\int \mathrm{d}^3 r\,\mathrm{d}^3 r' \frac{\rho_p(\boldsymbol{r})\rho_p(\boldsymbol{r}')}{|\boldsymbol{r}-\boldsymbol{r}'|} - \frac{3e^2}{4}\left(\frac{3}{\pi}\right)^{1/3}\int \mathrm{d}^3 r \rho_p^{4/3}(\boldsymbol{r}). \tag{6}$$

The pairing interaction is described by a zero-range, density-dependent force. The pairing energy density is expressed in terms of the pairing strength V_0, the saturation nucleon density ρ_0, and the parameter β, which gov-

erns the density dependence.

$$\mathcal{H}_{\rm pair} = \frac{1}{2} V_0 \left[1 - V_1 \left(\frac{\rho}{\rho_0}\right)^{\beta}\right] \sum_q \tilde{\rho}_q^{\dagger} \tilde{\rho}_q, \tag{7}$$

where V_1 represents the coupling of the volume ($V_1 = 0$) and surface ($V_1 = 1$) pairing contributions. To prevent mathematical divergences arising from zero-range pairing forces, pairing regularization can be applied, yielding finite, reliable predictions without artificially restricting the energy range considered. Here, we consider the pairing strengths $V_0 = -325$ MeV$\cdot$fm^3 for neutrons and -340 MeV$\cdot$fm^3 for protons [31, 44], with a mixed volume-surface pairing interaction ($V_1 = 0.5$) and a linear density dependence ($\beta = 1$), combined with a quasiparticle energy cutoff of $E_{\rm cut} = 60$ MeV. The cutoff $E_{\rm cut}$ enters through the pairing regularization, which replaces the constant pairing strength with a position-dependent effective strength computed locally from the density, effective mass, and cutoff to remove the divergent part of the energy [33]. In odd-even nuclei, pairing is treated by blocking the unpaired nucleon, excluding it from pairing correlations while the remaining nucleons form a paired condensate with the same pairing strengths and cutoff as in even-even systems. Near shell closures, pairing suppression is maximal and dominates over the influence of static deformation [45]. To describe pairing accurately in closed-shell nuclei, the Lipkin-Nogami (LN) correction is used. It corrects for the particle-number fluctuations inherent in the standard HFB approach [34]. The LN approximation serves as an approximate particle-number projection technique, restoring the symmetry violated by the HFB wave function. It removes spurious particle-number dispersion and improves the treatment of pairing correlations beyond the mean-field approximation. When implemented together with the HFB equations, the LN method yields improved nuclear properties and better agreement with experimental binding energies and pairing gaps [34, 45, 46].

Both the harmonic oscillator (HO) and transformed harmonic oscillator (THO) bases have been utilized to solve the HFB equations [32, 35]. The HO basis, defined by oscillator shells and deformation parameters, is efficient for well-bound nuclei, for which its Gaussian asymptotic behavior is sufficient. This justifies its use in the present work. For weakly bound and drip-line nuclei, the THO basis improves the representation of diffuse wave functions through coordinate transformation without drastically increasing basis size. The potential energy surfaces (PES) are generated by varying deformation parameters ($\beta_{2,4,6,8}$) to map out the energy landscape, revealing equilibrium shapes, barrier heights, and fission paths that are important for understanding collective excitations and decay processes. The utility of the adopted HFB framework extends beyond bulk properties to include microscopic single-particle spectra. Within the canonical basis, characterized by a diagonal density matrix ρ, single-particle states are described by canonical energies ϵ_i and occupation probabilities v_i^2. Excited and isomeric states are modeled by promoting quasiparticles or by applying the blocking prescription to specific orbitals within the HFB ground state [12, 39]. The blocking procedure, implemented self-consistently, induces a local modification of the pairing field, enabling the description of excited and long-lived metastable states, which play an important role in heavy-element α-decay spectroscopy.

Based on the PCM [37, 38], the α-decay half-life is calculated from the probability that a preformed α-particle tunnels through the Coulomb barrier between specified parent and daughter states,

$$T_{1/2}^{\alpha} = \frac{\hbar \ln 2}{S_{\alpha} \Gamma_{\alpha}}, \tag{8}$$

where S_{α} and Γ_{α} represent the α-preformation probability and the orientation-averaged decay width, respectively [47, 48],

$$\Gamma_{\alpha} = \frac{\hbar}{2} \int_0^{\pi} \nu(\theta) P(\theta) \sin\theta \, {\rm d}\theta. \tag{9}$$

The angle θ defines the direction of α emission relative to the symmetry axis of the deformed daughter nucleus, while $\nu(\theta)$ and $P(\theta)$ denote the assault frequency and barrier penetrability, respectively. Both are obtained from the Wentzel-Kramers-Brillouin (WKB) approximation [47–49] in terms of the local wave number, $k(R,\theta) = \sqrt{\frac{2\mu}{\hbar^2}\left|V_T(R,\theta) - Q_{\alpha}\right|}$.

Here, R is the center-of-mass distance between the α particle and the daughter nucleus, μ is their reduced mass, and $R_i(\theta)$ are the classical turning points satisfying $V_T = Q_{\alpha}$. The unobserved Q_{α} is derived from the present HFB(SLy4) masses and excitation energies to maintain consistency with the nuclear structure inputs and deformation parameters. Using the same EDF, Eq. (5), as for the evaluated nuclear structure, the total interaction potential is obtained as the energy difference between the combined α+daughter system and their separate energies, including a centrifugal contribution for unfavored decays,

$$V_T(R,\theta) = \int {\rm d}^3 r \left[\mathcal{H}(\rho_{\alpha}(\boldsymbol{r}) + \rho_D(\boldsymbol{r},R,\theta)) - \mathcal{H}(\rho_{\alpha}(\boldsymbol{r})) - \mathcal{H}(\rho_D(\boldsymbol{r}))\right] + \frac{\ell(\ell+1)\hbar^2}{2\mu R^2}. \tag{10}$$

The transferred orbital angular momentum (ℓ) is constrained by the conservation of angular momentum,

$|J_P - J_D| \leqslant \ell \leqslant |J_P + J_D|$, and by parity, $\pi_P = (-1)^\ell \pi_D$, where $J_{P,D}$ and $\pi_{P,D}$ denote the spins and parities of the parent (P) and daughter (D) nuclei. Since the α-particle has a strongly correlated few-body nature that lies beyond the HFB mean-field framework designed for medium and heavy nuclei, we instead adopt its empirical Gaussian density distribution [50], fitted to electron scattering data, $\rho_\alpha(r) = 0.4229\,\mathrm{e}^{-0.7024r^2}$.

The spectroscopic-preformation factor S_α is given by a semi-empirical formula [38, 51] that incorporates the important [52−54] shell effects, pairing, and spin-parity configurations of parent and daughter nuclei, with parameters optimized [49, 55, 56] to reproduce experimental half-lives across a wide range of favored and unfavored decays,

$$S_\alpha = \Big[\mathcal{A}_0 \exp\Big(-0.003\,(Z - Z_0 - Z_c)^2 - 0.006\,(N - N_0 - N_c)^2\Big) - a_p\Big]\mathrm{H}_\ell. \tag{11}$$

This formulation uses the parent's Z and N, the shell closures Z_0 and N_0, and the particle numbers beyond them (Z_c and N_c) at which S_α peaks. For even-Z, odd-N nuclei, a category that includes the nuclei examined in this work, the pairing factor is $a_p = 0.0056(N - N_0)^{1/3}$. The hindrance factor for unfavored decays is $\mathrm{H}_\ell = \exp(1 - n - 0.6\Delta J)$, where n is the order of a given J_D state in the daughter's spectrum, with $n = 1$ for the first such state, and $\Delta J = |J_D - J_P|$ is the spin difference.

Given a total α-decay branching ratio $B_\alpha(\%)$, a partial branching ratio to a specific daughter state J_D^π is

$$b_\alpha\left(J_D^\pi\right) = \frac{T_\alpha^{\mathrm{Total}} \times B_\alpha}{T_\alpha\left(J_D^\pi\right)}, \tag{12}$$

where $T_\alpha^{\mathrm{Total}} = \left[\sum_{J_D^\pi} \frac{1}{T_\alpha\left(J_D^\pi\right)}\right]^{-1}$. By integrating microscopic HFB-Skyrme structure, WKB tunneling, and a semi-empirical spectroscopic preformation factor, the present PCM framework quantitatively predicts α-decay observables, including half-lives, fine-structure branching ratios, and hindrance factors, for decay modes leading to deformed and excited daughter nuclei.

III. RESULTS AND DISCUSSION

Using the PCM with the Skyrme-SLy4 potential, WKB tunneling, and the semi-empirical spectroscopic-preformation factor from Eq. (11), we calculated the partial α-decay half-lives ($T_{\alpha i}^{\mathrm{cal}}$) and branching ratios ($b_{\alpha i}^{\mathrm{cal}}(\%)$) for the sequence of even-odd isotopes comprising the $^{295,297,299,301,303}120$ α-decay chains. Table 1 lists the obtained estimates for decays to the ground state (GS) and to the first low-lying excited states of the produced daughter nuclei. These results are based on HFB(SLy4) structural inputs, including the spin-parities and energies of the involved states (columns 1-3), deformation parameters of the daughter nuclei, and the Q_α values for the unobserved decays. To obtain these structural properties, we carried out self-consistent mean-field calculations using the HFB method [32−35], based on the Skyrme-SLy4 EDF of the effective NN interaction and a zero-range pairing interaction, with wave functions represented in a harmonic-oscillator basis. The total energy surfaces were computed across a multidimensional deformation space for axially deformed configurations to investigate their ground-state properties and the associated excited states. The Q_α values for the ground-state to ground-state decay modes are taken from AME2021 [57] where observed, and derived from the obtained HFB(SLy4) masses otherwise. The states considered in the daughter nuclei comprise the GS and the first two excited states. An additional third excited state is included when its estimated energy is low. Column 6 of Table I presents the key quadrupole deformation parameters β_{2D} for the daughter nuclei as obtained from the HFB(SLy4) calculations. Column 4 provides the minimum angular momentum Δl for unfavored α-decays. Where available, we use the observed spontaneous fission half-life and total α-branching ratio to constrain our calculations of partial branching ratios. For benchmarking, we compare against measured α-decay half-lives [58, 59]. For isotopes with no observed fission, partial α-branching ratios are computed relative to one another.

The spin-parity of the even-odd nucleus is determined by the quantum numbers of its unpaired quasi-neutrons. While the GS corresponds to the blocked quasineutron configuration that minimizes the total energy, the excited states are identified by blocking higher-energy quasineutron states, with each unique blocking providing the spin-parity for a distinct excited state. We calculated the excitation energy from the total energy difference between states, which includes the energy from full nuclear rearrangement. The difference in quasiparticle energy gives the cost of exciting a single nucleon, but it omits the energy contribution from these systematic rearrangements. The robustness of the selected blocked quasiparticle configurations warrants careful consideration. In odd-mass nuclei, blocking different quasineutron states can yield several self-consistent solutions with comparable energies, especially when orbitals are densely packed near the Fermi surface. To assess reliability, we confirmed that the selected configuration corresponds to the minimum total energy, with an energy separation from the nearest competing state. In the transitional region near the prolate-to-oblate shape transition, where the level density rises, configuration mixing may become non-negligible. However, we tested the impact of alternative blocking choices on the calculated α-decay observables.

Table 1. The calculated partial ($T^{\rm cal}_{\alpha i}$) and total ($T^{\rm cal}_{\alpha}$) α-decay half-lives and corresponding branching ratios $b^{\rm cal}_{\alpha i}$ (J^{π}_{D}), within the PCM framework, across the even-odd $^{295-303}$120 chains, covering both the GS to GS transitions and decays to low-lying excited states in daughter nuclei, as derived and their energy (E^{π}_{J}) from the current HFB(SLy4) calculations that also yield the daughter deformations (β_{2D}). The Q_{α} values in column 5 are primarily from the AME2021 mass tables [57]. Values in parentheses are from our current HFB(SLy4) calculations, which were used when no value was available in AME2021 or it is a systematic value showing a significant deviation from other HFB and MM models and the present calculation. The α-decay width is computed using the WKB penetrability and assault frequency from the Skyrme-SLy4 EDF, along with the spectroscopic factor S_{α} from Eq. (11) and the minimum allowed α-particle angular momentum Δl. The calculated $b^{\rm cal}_{\alpha i}$ utilizes the experimental total α branching $B^{\rm exp}_{\alpha}$ and the observed SF ($T^{\rm exp}_{SF}$, $B^{\rm exp}_{SF}$), when available. Observed half-lives for α-decay ($T^{\rm exp}_{\alpha}$) and SF [58, 59], as well as their branching ratios, are listed for comparison.

Parent(gs)	Daughter (J^{π}_{D})	E^{π}_{J} (D) /MeV	Δl ($\hbar$)	Q_{α}/MeV from AME2021 or calculated	β_{2D}	S_{α} Eq. (11)	$T^{\rm cal}_{\alpha i}(J^{\pi}_{D})$/s	$T^{\rm cal(exp)}_{\alpha}$, $T^{\rm exp}_{SF}$/s	$b^{\rm cal}_{\alpha i}(J^{\pi}_{D})$ (%)	$B^{\rm exp}_{\alpha(SF)}$ (%)
				^{295}120 chain						
^{295}120(1/2^{+})	^{291}Og(5/2^{+})	0	2	(12.491)	0.120	0.021	2.102×10^{-4}	3.341×10^{-5}	15.90	
	(3/2^{+})	0.006	2	(12.483)		0.038	1.208×10^{-4}		27.65	
	(1/2^{+})	0.088	0	(12.403)		0.070	5.918×10^{-5}		56.45	
^{291}Og(5/2^{+})	^{287}Lv(1/2^{+})	0	2	(12.434)	0.138	0.026	8.033×10^{-5}	1.846×10^{-5}	22.98	
(3/2^{+})	(1/2^{+})	0	2	(12.440)		0.048	7.337×10^{-5}		25.16	
(5/2^{+})	(3/2^{+})	0.193	2	(12.241)		0.048	1.189×10^{-4}		15.53	
(3/2^{+})	(3/2^{+})	0.193	0	(12.247)		0.087	6.117×10^{-5}		30.19	
(5/2^{+})	(9/2^{+})	0.204	2	(12.230)		0.026	3.908×10^{-4}		4.72	
(3/2^{+})	(9/2^{+})	0.204	4	(12.236)		0.014	1.304×10^{-3}		1.42	
^{287}Lv(1/2^{+})	^{283}Fl(9/2^{+})	0	4	(11.815)	0.170	0.009	6.089×10^{-3}	7.730×10^{-5}	1.27	
	(1/2^{+})	0.009	0	(11.806)		0.099	1.061×10^{-4}		72.86	
	(3/2^{+})	0.043	2	(11.772)		0.054	4.104×10^{-4}		18.83	
	(5/2^{+})	0.109	2	(11.706)		0.030	1.099×10^{-3}		7.03	
^{283}Fl(9/2^{+})	^{279}Cn(3/2^{+})	0	2	(11.654)	0.199	0.017	9.935×10^{-4}	5.834×10^{-5}	5.87	
(1/2^{+})	(3/2^{+})		4	(11.663)		0.057	3.046×10^{-4}		19.16	
(9/2^{+})	(5/2^{+})	0.058	2	(11.596)		0.031	5.210×10^{-4}		11.20	
(1/2^{+})	(5/2^{+})		2	(11.605)		0.031	4.977×10^{-4}		11.72	
(9/2^{+})	(1/2^{+})	0.159	4	(11.495)		0.009	1.343×10^{-2}		0.43	
(1/2^{+})	(1/2^{+})		0	(11.504)		0.104	2.161×10^{-4}		27.00	
(9/2^{+})	(9/2^{+})	0.170	0	(11.484)		0.104	2.412×10^{-4}		24.19	
(1/2^{+})	(9/2^{+})		4	(11.493)		0.009	1.347×10^{-2}		0.43	
^{279}Cn(3/2^{+})	^{275}Ds(3/2^{+})	0	0	(11.440)	0.221	0.266	3.037×10^{-5}	2.535×10^{-5}	83.48	
	(5/2^{+})	0.079	2	(11.361)		0.146	1.557×10^{-4}		16.28	
	(13/2^{-})	0.167	5	(11.273)		0.013	1.075×10^{-2}		0.24	
^{275}Ds(3/2^{+})	^{271}Hs(3/2^{+})	0	0	(11.550)	0.237	0.263	5.328×10^{-6}	4.471×10^{-6}	83.92	
	(5/2^{+})	0.106	2	(11.444)		0.144	2.819×10^{-5}		15.86	
	(13/2^{-})	0.201	5	(11.349)		0.013	2.040×10^{-3}		0.22	
^{271}Hs(3/2^{+})	^{267}Sg(11/2^{-})	0	5	(9.766)	0.249	0.022	1.194	0.336	28.11	
	(9/2^{+})	0.107	4	(9.659)		0.040	0.882		38.04	
	(7/2^{+})	0.260	2	(9.506)		0.073	0.991		33.85	
^{267}Sg(11/2^{-})	^{263}Rf(9/2^{+})	0	1	(8.630)	0.258	0.113	85.879	67.760	13.41	
	(7/2^{+})	0.017	3	(8.613)		0.062	321.169	$T^{\rm exp}_{\alpha}=108.000\pm42.000$	3.59	17

Continued on next page

Table 1-continued from previous page

Parent(gs)	Daughter (J^π_D)	E^π_J (D) /MeV	Δl ($\hbar$)	Q_α/MeV from AME2021 or calculated	β_{2D}	S_α Eq. (11)	$T^{\rm cal}_{\alpha i}(J^\pi_D)$/s	$T^{\rm cal(exp)}_\alpha$, $T^{\rm exp}_{SF}$/s	$b^{\rm cal}_{\alpha i}(J^\pi_D)$ (%)	$B^{\rm exp}_{\alpha(SF)}$ (%)
								$T^{\rm exp}_{SF}=130.120\pm50.602$		$B^{\rm exp}_{SF}\approx83$
^{263}Rf								$T^{\rm exp}_{SF}=817.800\pm444.600$		$B^{\rm exp}_{SF}\approx100$
					^{297}120 chain					
$^{297}120(1/2^+)$	^{293}Og$(1/2^+)$	0	0	(12.331)	0.101	0.051	2.006×10^{-4}	1.467×10^{-4}	73.13	
	$(3/2^+)$	0.057	2	(12.274)		0.028	8.490×10^{-4}		17.28	
	$(5/2^+)$	0.172	2	(12.159)		0.015	1.529×10^{-3}		9.59	
^{293}Og$(1/2^+)$	^{289}Lv$(1/2^+)$	0	0	(11.723)	0.118	0.069	6.043×10^{-4}	5.831×10^{-4}	96.48	
	$(15/2^-)$	0.218	7	(11.505)		0.001	0.489		0.12	
	$(3/2^+)$	0.410	2	(11.313)		0.038	0.017		3.40	
^{289}Lv$(1/2^+)$	^{285}Fl$(1/2^+)$	0	0	(11.337)	0.150	0.084	1.335×10^{-3}	1.225×10^{-3}	91.80	
	$(15/2^-)$	0.195	7	(11.142)		0.001	1.052		0.12	
	$(3/2^+)$	0.205	2	(11.132)		0.046	0.015		8.08	
^{285}Fl$(1/2^+)$	^{281}Cn$(1/2^+)$	0	0	10.560	0.182	0.093	0.038	0.028	74.31	
	$(9/2^+)$	0.007	4	10.553		0.008	1.782	$T^{\rm exp}_\alpha=0.210\pm0.100$	1.59	≈100
	$(3/2^+)$	0.050	2	10.510		0.051	0.150		18.88	$B^{\rm exp}_{SF}<100$
	$(5/2^+)$	0.117	2	10.436		0.028	0.542		5.22	
^{281}Cn$(1/2^+)$	^{277}Ds$(3/2^+)$	0	2	10.430	0.210	0.131	0.059	0.011	19.16	
$(9/2^+)$			4	10.437		0.039	0.070	$T^{\rm exp}_\alpha=0.180\pm0.080$	16.08	≈100
$(1/2^+)$	$(5/2^+)$	0.063	2	10.367		0.072	0.092		12.19	
$(9/2^+)$			2	10.374		0.072	0.088		12.72	
$(1/2^+)$	$(1/2^+)$	0.169	0	10.261		0.239	0.064		17.58	
$(9/2^+)$			4	10.268		0.022	0.239		3.84	
$(1/2^+)$	$(9/2^+)$	0.194	4	10.236		0.022	0.413		2.72	
$(9/2^+)$			0	10.243		0.239	0.072		15.71	
^{277}Ds$(3/2^+)$	^{273}Hs$(3/2^+)$	0	0	(10.586)	0.229	0.249	8.260×10^{-4}	0.001	92.63	
	$(5/2^+)$	0.094	2	(10.492)		0.137	0.010	$T^{\rm exp}_\alpha=0.006\pm0.003$	7.37	≈100
^{273}Hs$(3/2^+)$	^{269}Sg$(3/2^+)$	0	0	9.650	0.242	0.241	0.097	0.082	84.38	
	$(5/2^+)$	0.122	2	9.528		0.132	0.766	$T^{\rm exp}_\alpha=1.060\pm0.500$	10.64	≈100
	$(11/2^-)$	0.231	5	9.419		0.022	1.636		4.98	
^{269}Sg$(3/2^+)$	^{265}Rf$(11/2^-)$	0	5	8.580	0.252	0.020	141.793	110.490	77.92	
	$(9/2^+)$	0.091	4	8.489		0.035	711.060	$T^{\rm exp}_\alpha=300.000\pm120.000$	15.54	≈100
	$(7/2^+)$	0.267	2	8.315			1.690×10^{3}		6.54	
^{265}Rf								$T^{\rm exp}_{SF}=96.000\pm36.000$		$B^{\rm exp}_{SF}\approx100$
					^{299}120 chain					
$^{299}120(1/2^+)$	^{295}Og$(1/2^+)$	0	0	(12.079)	−0.097	0.034	5.981×10^{-4}	4.999×10^{-4}	83.57	
	$(3/2^+)$	0.134	2	(11.945)		0.019	3.915×10^{-3}		12.77	
	$(3/2^+)$	0.183	2	(11.896)		0.007	0.014		3.66	
^{295}Og$(1/2^+)$	^{291}Lv$(1/2^+)$	0	0	(11.318)	−0.110	0.050	0.013	0.010	74.80	

Continued on next page

Table 1-continued from previous page

Parent(gs)	Daughter (J_D^π)	E_J^π (D) /MeV	Δl ($\hbar$)	Q_α/MeV from AME2021 or calculated	β_{2D}	S_α Eq. (11)	$T_{\alpha i}^{\rm cal}(J_D^\pi)$/s	$T_\alpha^{\rm cal(exp)}$, $T_{SF}^{\rm exp}$/s	$b_{\alpha i}^{\rm cal}(J_D^\pi)$ (%)	$B_{\alpha(SF)}^{\rm exp}$ (%)
	$(3/2^+)$	0.051	2	(11.267)		0.027	0.054	$T_\alpha^{\rm exp}=0.680\pm0.540$	18.32	
	$(5/2^+)$	0.162	2	(11.156)		0.015	0.145		6.88	
^{291}Lv$(1/2^+)$	^{287}Fl$(1/2^+)$	0	0	10.890	0.130	0.066	0.019	0.018	96.67	
	$(15/2^-)$	0.274	7	10.616		0.001	16.317	$T_\alpha^{\rm exp}=0.026\pm0.012$	0.11	≈ 100
	$(3/2^+)$	0.416	2	10.474		0.036	0.557		3.22	
^{287}Fl$(1/2^+)$	^{283}Cn$(1/2^+)$	0	0	10.170	0.160	0.078	0.432	0.390	90.28	
	$(3/2^+)$	0.195	2	9.975		0.043	4.255	$T_\alpha^{\rm exp}=0.510\pm0.120$	9.16	≈ 100
	$(9/2^+)$	0.202	4	9.968		0.007	69.156		0.56	
^{283}Cn$(1/2^+)$	^{279}Ds$(1/2^+)$	0	0	9.890	0.194	0.205	0.284	0.218	65.13	
	$(9/2^+)$	0.019	4	9.871		0.019	16.379	$T_\alpha^{\rm exp}=5.588\pm1.000$	1.13	85
	$(3/2^+)$	0.061	2	9.829		0.113	1.347	$T_{SF}^{\rm exp}=31.667\pm5.667$	13.75	$B_{SF}^{\rm exp}=15$
	$(5/2^+)$	0.125	2	9.765		0.062	3.716		4.99	
^{279}Ds$(1/2^+)$	^{275}Hs$(3/2^+)$	0	2	10.110	0.219	0.124	0.031	0.014	$5.32\pm2.21.63$	
	$(5/2^+)$	0.074	2	10.036		0.068	0.094	$T_\alpha^{\rm exp}=1.750\pm0.800$	1.77 ± 0.74	12 ± 5
	$(9/2^+)$	0.196	4	9.914		0.020	2.777	$T_{SF}^{\rm exp}=0.239\pm0.800$	0.06 ± 0.03	$B_{SF}^{\rm exp}\approx 88\pm5$
	$(1/2^+)$	0.196	0	9.914		0.225	0.034		4.85 ± 2.02	
^{275}Hs$(3/2^+)$	^{271}Sg$(3/2^+)$	0	0	9.450	0.235	0.228	0.776	0.591	76.14	100
	$(5/2^+)$	0.110	2	9.340		0.125	2.476	$T_\alpha^{\rm exp}=0.280\pm0.130$	23.86	
^{271}Sg$(3/2^+)$	^{267}Rf$(3/2^+)$	0	0	(8.583)	0.245	0.214	55.540	32.120	24.29 ± 13.30	
	$(5/2^+)$	0.140	2	(8.443)		0.117	81.634	$T_\alpha^{\rm exp}=314.286\pm286.957$	16.53 ± 9.05	42 ± 23
	$(11/2^-)$	0.154	5	(8.429)		0.019	1.138×10^3	$T_{SF}^{\rm exp}=227.586\pm286.957$	1.19 ± 0.65	$B_{SF}^{\rm exp}\approx 58\pm23$
^{267}Rf								$T_{SF}^{\rm exp}=(9.000\pm5.400)\times10^3$		$B_{SF}^{\rm exp}=100$
					^{301}120 chain					
^{301}120$(1/2^+)$	^{297}Og$(1/2^+)$	0	0	(11.691)	−0.071	0.019	0.010	8.094×10^{-3}	77.35	
	$(3/2^+)$	0.069	2	(11.622)		0.010	0.048		16.96	
	$(1/2^+)$	0.142	2	(11.549)		0.004	0.112		5.69	
^{297}Og$(1/2^+)$	^{293}Lv$(3/2^+)$	0	2	(11.203)	−0.092	0.018	0.100	0.033	32.79	
	$(3/2^+)$	0.013	2	(11.190)		0.007	0.283		11.58	
	$(1/2^+)$	0.122	0	(11.081)		0.033	0.059		55.63	
^{293}Lv$(3/2^+)$	^{289}Fl$(1/2^+)$	0	2	10.680	−0.116	0.026	0.463	0.127	27.42	
	$(3/2^+)$	0.051	0	10.629		0.048	0.211	$T_\alpha^{\rm exp}=0.113\pm0.045$	60.33	≈ 100
	$(5/2^+)$	0.160	2	10.520		0.026	1.038		12.25	
^{289}Fl$(1/2^+)$	^{285}Cn$(1/2^+)$	0	0	9.950	0.138	0.061	1.858	1.819	97.94	
	$(15/2^-)$	0.297	7	9.653		0.001	1.500×10^3	$T_\alpha^{\rm exp}=2.100\pm0.600$	0.12	≈ 100
	$(3/2^+)$	0.396	2	9.554		0.033	93.615		1.94	
^{285}Cn$(1/2^+)$	^{281}Ds$(1/2^+)$	0	0	9.390	0.171	0.166	29.332	26.107	89.01	
	$(9/2^+)$	0.189	4	9.201		0.015	2.567×10^3	$T_\alpha^{\rm exp}=30.000\pm8.000$	1.02	≈ 100
	$(3/2^+)$	0.202	2	9.188		0.091	332.025		7.86	

Continued on next page

Table 1-continued from previous page

Parent(gs)	Daughter (J^π_D)	E^π_J (D) /MeV	Δl ($\hbar$)	Q_α/MeV from AME2021 or calculated	β_{2D}	S_α Eq. (11)	$T^{\rm cal}_{\alpha i}(J^\pi_D)$/s	$T^{\rm cal(exp)}_\alpha$, $T^{\rm exp}_{SF}$/s	$b^{\rm cal}_{\alpha i}(J^\pi_D)$ (%)	$B^{\rm exp}_{\alpha(SF)}$ (%)
	$(5/2^+)$	0.289	2	9.101		0.050	1.235×10^3		2.11	
^{281}Ds$(1/2^+)$	^{277}Hs$(1/2^+)$	0	0	9.470	0.205	0.192	0.943	0.776	8.23 ± 5.76	
	$(9/2^+)$	0.021	4	9.449		0.017	64.461	$T^{\rm exp}_\alpha = 140.000\pm42.857$	0.12 ± 0.08	10 ± 7
	$(3/2^+)$	0.048	2	9.422		0.105	4.693	$T^{\rm exp}_{SF} = 15.556\pm42.857$	1.65 ± 1.16	$B^{\rm exp}_{SF}\approx90\pm7$
^{277}Hs$(1/2^+)$	^{273}Sg$(3/2^+)$	0	2	(9.234)	0.225	0.113	3.121	$T^{cal}_\alpha = 2.382$	0.38	
	$(5/2^+)$	0.086	2	(9.148)		0.062	10.064	$T^{\rm exp}_{SF} = 0.012\pm0.009$	0.12	$B^{\rm exp}_{SF}\approx100$
^{273}Sg$(3/2^+)$	^{269}Rf$(3/2^+)$	0	0	(8.437)	0.236	0.203	375.350	269.167	71.71	
	$(5/2^+)$	0.125	2	(8.312)		0.111	1.001×10^3		26.89	
	$(9/2^+)$	0.245	4	(8.192)		0.033	1.919×10^4		1.40	
					^{303}120 chain					
^{303}120$(1/2^+)$	^{299}Og$(1/2^+)$	0	0	(11.872)	−0.030	0.007	5.750×10^{-3}	4.741×10^{-3}	82.46	
	$(3/2^+)$	0.102	2	(11.770)		0.004	0.027		17.54	
^{299}Og$(1/2^+)$	^{295}Lv$(3/2^+)$	0	2	(10.816)	−0.055	0.010	1.053	0.280	26.61	
	$(1/2^+)$	0.032	0	(10.784)		0.018	0.416		67.43	
	$(1/2^+)$	0.262	0	(10.554)		0.007	4.705		5.96	
^{295}Lv$(3/2^+)$	^{291}Fl$(1/2^+)$	0	2	(10.004)	−0.099	0.017	31.679	19.576	61.79	
	$(3/2^+)$	0.224	0	(9.780)		0.031	51.238		38.21	
^{291}Fl$(1/2^+)$	^{287}Cn$(1/2^+)$	0	0	(9.316)	−0.122	0.044	175.659	148.981	84.81	
	$(3/2^+)$	0.045	2	(9.271)		0.024	1.276×10^3		11.67	
	$(5/2^+)$	0.145	2	(9.171)		0.013	4.238×10^3		3.52	
^{287}Cn$(1/2^+)$	^{283}Ds$(1/2^+)$	0	0	9.120	0.144	0.127	232.327	226.437	97.46	
	$(15/2^-)$	0.317	7	8.803		0.002	2.834×10^5		0.08	
	$(3/2^+)$	0.371	2	8.749		0.070	9.222×10^3		2.46	
^{283}Ds$(1/2^+)$	^{279}Hs$(1/2^+)$	0	0	(8.959)	0.181	0.155	46.206	45.118	97.64	
	$(9/2^+)$	0.173	4	(8.786)		0.014	3.340×10^3		1.35	
	$(3/2^+)$	0.212	2	(8.747)		0.047	4.488×10^3		1.01	
^{279}Hs$(1/2^+)$	^{275}Sg$(1/2^+)$	0	0	(8.780)	0.210	0.175	29.646	17.526	59.12	
	$(9/2^+)$	0.006	4	(8.774)		0.016	1.775×10^3		0.99	
	$(3/2^+)$	0.023	2	(8.757)		0.096	51.016		34.35	
	$(5/2^+)$	0.089	2	(8.691)		0.053	316.400		5.54	
^{275}Sg$(1/2^+)$	^{271}Rf$(3/2^+)$	0	2	(8.197)	0.226	0.100	2.003×10^3	810.865	40.49	
$(9/2^+)$	$(3/2^+)$	0	4	(8.203)		0.030	2.361×10^4		3.43	
$(1/2^+)$	$(5/2^+)$	0.097	2	(8.100)		0.055	9.324×10^3		8.70	
$(9/2^+)$	$(5/2^+)$	0.097	2	(8.106)		0.055	8.878×10^3		9.13	
$(1/2^+)$	$(9/2^+)$	0.129	4	(8.068)		0.017	4.671×10^4		1.74	
$(9/2^+)$	$(9/2^+)$	0.129	0	(8.074)		0.183	2.221×10^3		36.51	

As shown in Table 1, the estimated single-particle neutron orbitals near the Fermi surface show dominant $1/2^+$ and $3/2^+$ levels as the neutron number approaches $N = 184$, with increasing complexity as Z decreases. The $1/2^+$ ($3/2^+$) spin-parity configuration appears 27 (14) times as an estimated ground state for isotopes with $N = 169$–183 (163–179), and 8 (25) times as the first or second low-lying excited state. The $9/2^+$ spin-parity con-

figuration is identified as GS in three nuclei with $N = 159$ and 169, and as a lower excited state in 11 isotopes. The $5/2^+$ assignment is estimated once as a probable GS for $N = 173$ and 12 times as the lowest excited state, while the $15/2^-$ state is estimated four times as the lowest excited state for $N = 173$. Furthermore, the $11/2^-$ configuration is identified as GS in two isotopes with $N = 161$, and the $7/2^+$ state is indicated once as the first excited state for $N = 159$. The inferred sequence of neutron orbital filling from $N = 159$ to the shell closure at $N = 184$ reveals a clear evolution of shell structure. This begins with the occupation of high-spin orbitals ($7/2^+$, $11/2^-$, $9/2^+$) above the $N = 126$ core. As neutrons are added, the ground-state spins systematically decrease. Upon approaching the magic number $N = 184$, the ground states become almost exclusively low spin, ending with the classic signature of filling the last $4s_{1/2}$ and $3d_{3/2}$ orbitals in a spherical shell. This progression from high-spin to low-spin states is consistent with theoretical predictions of a shell closure at $N = 184$ and highlights the role of deformation and residual interactions in reordering single-particle levels in SHN. Occasionally, the ground-state spin-parity assignment remains ambiguous because the calculated energy differences between competing configurations are less than 10 keV, which is within the margin of numerical uncertainties. Examples include ^{291}Og($5/2^+$, $3/2^+$), ^{283}Fl($9/2^+$,$1/2^+$), ^{281}Cn($1/2^+$,$9/2^+$), and ^{275}Sg($1/2^+$, $9/2^+$).

As nuclei are populated beyond the indicated neutron energy gap at $N = 152$ [60], they continue to evolve structurally, progressively adopting more deformed shapes. The observed ground and excited states below 100 keV indicate that the lowest-energy orbitals available for neutrons immediately above $N = 152$ are $\nu 1/2^+[620](2g_{7/2^+})$ and $3/2^+[622](3d_{5/2^+})$. With further neutron addition, the $7/2^+[613](1i_{11/2^+})$ orbital is occupied in the $N = 155$ and 157 isotones, followed by the appearance of a $9/2^+$ ground state at $N = 157$. The present calculations identify this state, which extends to $N = 159$ and is associated with a large prolate deformation up to $\beta_2 \approx 0.26$, as the deformed $9/2^+[615]$ orbital originating from the spherical $2g_{9/2^+}$ state. The next appearing $11/2^-[725](1j_{15/2^-})$ state, calculated to be the ground state for $N = 161$ isotones in Table I, is likely the same state observed as a low-lying excitation in $N = 151$ isotones [58]. The $3/2^+[611](2g_{7/2^+})$ state starts to appear as the ground state at odd $N = 163-167$ with β_2 deformation between 0.2 and 0.25. In this deformation range, it lies above the $9/2^+[615]$ and $11/2^-[725]$ states. As β_2 decreases, its energy rises, and by $N = 169$ ($\beta_2 = 0.12-0.21$) it shifts to become the first or second excited state for $N = 169-171$. The $5/2^+[613](3d_{5/2^+})$ state follows the $3/2^+[611]$ state in energy for these prolate deformations, succeeded by the $9/2^+[604](1i_{11/2^+})$ and then the $1/2^+[611](4s_{1/2^+})$ states. A notable rearrangement of the order of energy levels occurs around $N = 168$ near $\beta_2 \approx 0.2$. The energy of the $3/2^+[611]$ state continues to increase as β_2 decreases, reaching nonprincipal low-lying levels at $N = 179-183$, where the nucleus exhibits a weak oblate deformation with β_2 magnitude less than -0.06.

With a prolate deformation of $\beta_2 = 0.12-0.21$, the level ordering shifts within $N = 169-171$ such that $1/2^+[611]$ becomes the lowest state, followed by $9/2^+[604]$, then $3/2^+[611]$, and finally $5/2^+[613]$, which becomes the highest relative to them in this region. This explains the appearance of the $1/2^+[611]$ assignment as the ground state for 13 nuclei with odd $N = 169-173$, and the frequent appearance of the $9/2^+[604]$ state as the first excited state for $N = 169$ and 171, and as the second low-lying excited state for $N = 165$ and 167 ($\beta_2 = 0.20-0.24$), below $1/2^+[611]$, which appears as the second and third excited states in this region. The state $1/2^+[611]$ with weak oblate shape ($\beta_2 = -0.06$ to -0.07) reappears as an excited state of higher energy at $N = 179$. For $N = 173$ ($\beta_2 = 0.12-0.14$), the state $15/2^-[707](1j_{15/2^-})$ comes next to $1/2^+[611]$.

Calculations for $N = 175$ indicate a neutron occupation sequence of $1/2^+[640](1i_{11/2^+})$, followed by $3/2^+[642](2g_{9/2^+})$ and $5/2^+[642](1i_{13/2^+})$ states, with relatively strong oblate deformation, and then $1/2^+[600](3d_{3/2^+})$. The favored state shifts with decreasing oblate deformation. The $1/2^+[620](2g_{7/2^+})$ state becomes preferred for $N = 175$ and 177 with weaker oblate deformations than $\beta_2 = -0.12$. In the range from $\beta_2 = -0.06$ to -0.09, the $3/2^+[651](1i_{13/2^+})$ configuration becomes favored for $N = 177$ and 179, alternating in dominance with $1/2^+[651](2g_{9/2^+})$ for $N = 177$ and $1/2^+[660](1i_{13/2^+})$ for $N = 179$. The $1/2^+[600](3d_{3/2^+})$ orbital persistently appears among the lowest states starting from $N = 173$ until it becomes the favored ground state as N approaches 184, corresponding to spherical or very weakly oblate deformed nuclei, followed by $3/2^+[603](3d_{3/2^+})$, and then $3/2^+[611](2g_{7/2^+})$ and $1/2^+[631](3d_{5/2^+})$.

As an example, Fig. 1 displays the neutron single-particle spectrum around the Fermi surface for the essentially spherical $^{303}120_{183}$ nucleus as derived from the present self-consistent calculations. The level ordering shown in Fig. 1 follows the Nilsson sequence expected for weakly oblate nuclei in the vicinity of the Fermi surface, with the main deeply occupied levels (black) arranged from lowest to highest energy. The final occupied neutron orbital in GS, $1/2^+[600]3d_{3/2^+}$, is highlighted in blue, giving the estimated ground-state spin-parity assignment of the odd neutron. The unoccupied levels above (red) serve as estimates for the low-lying excited configurations. Although the GS of ^{303}120 is spherical, the weak oblate deformation present in its excited states induces a moderate splitting of the spherical orbitals, and the resulting level ordering is well reproduced by the Nilsson

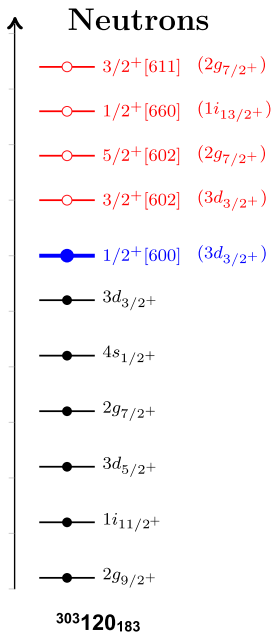

Fig. 1. (color online) Neutron single-particle levels near the Fermi surface of the nearly spherical $^{303}120(N=183)$ nucleus, obtained from HFBTHO calculations using the SLY4 Skyrme functional and the Lipkin-Nogami pairing prescription to account for particle-number fluctuations in the odd-mass system. The unpaired neutron was treated using the blocking approximation. Occupied levels are shown in black, the last occupied state in blue, and unoccupied (excited-state) levels in red. The corresponding Nilsson quantum numbers for the excited states and the spherical orbitals are indicated.

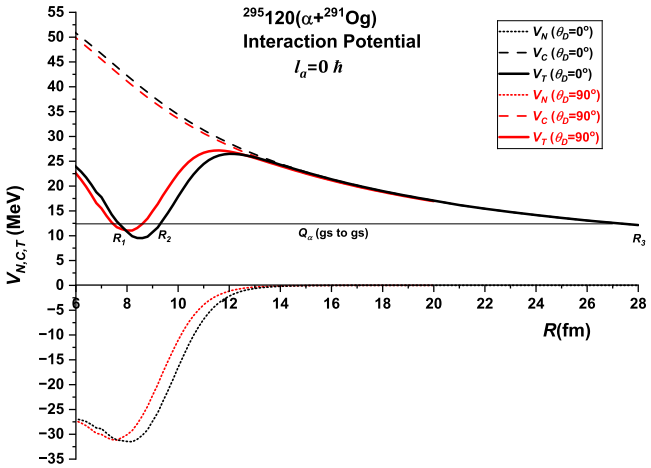

Fig. 2. (color online) The nuclear (V_N), Coulomb (V_C), and total (V_T) potentials for the α-^{291}Og system inside the parent $^{295}120$ nucleus are shown as functions of the center-of-mass separation R. The calculations were performed for two orientations of the prolate-deformed daughter nucleus ^{291}Og ($\beta_2=0.12$): $\theta=0°$ (black curves) and $\theta=90°$ (red curves). Also indicated are the three classical turning points $R_{1,2,3}$ and the Q_α-value for the favored ($\ell_\alpha=0\hbar$) decay mode.

scheme.

Concerning the stability of the α-decay chains under investigation, Fig. 2 illustrates the total interaction potential for the α-^{291}Og clusters inside $^{295}120$ at two orientations $\theta=0°$ and $\theta=90°$ of the prolate deformed daughter nucleus ^{291}Og ($\beta_2=0.12$). The orientation-averaged decay width, computed via Eq. (9) by averaging between these two optimum angles, effectively accounts for the reflection-symmetry character of the prolate deformation. The plot shows that, for prolate deformation, the penetration probability increases from $\theta=90°$ to $\theta=0°$, owing to a reduced barrier width (R_3-R_2) and a lower Coulomb barrier in the axial direction. This highlights the strong influence of nuclear deformation on the tunneling dynamics, with emission along the symmetry axis being substantially favored over the equatorial direction.

Table I shows that the decays of $^{295}120$, ^{291,297,299}Og, ^{271}Hs, ^{287,293}Lv, and ^{283}Fl are less likely to proceed directly to the GS of the daughter nucleus. Instead, decay via excited states is much more probable, leading to shorter partial half-lives and larger branching ratios. The decays from these isotopes preferentially populate the $1/2^+$ state (in ^{291}Og, ^{293,295}Lv, ^{283}Fl, ^{279}Cn), the $3/2^+$ state in ^{287}Lv and ^{289}Fl, and the $9/2^+$ state of ^{267}Sg. Richer decay schemes are predicted for ^{291}Og, ^{283}Fl, ^{281}Cn, and ^{275}Sg, with more than five distinct decay modes estimated. The predicted decay chains under study are longer than the corresponding even-even chains [11], with the number of odd neutrons increasing toward the shell closure. While the $^{301}120$ chain is predicted to terminate at ^{277}Hs ($B_{SF}^{\rm exp}\approx 100\%$), the $^{295,297,299}120$ chains are expected to extend down to ^{263,265,267}Rf. The $^{303}120$ chain is expected to terminate at ^{279}Hs, which is expected to undergo rapid spontaneous fission, as indicated in [11] and references therein.

Among 22 predicted half-lives in Table I for isotopes that are either not yet synthesized or have no observed α-decay, relatively long half-lives are estimated for $^{301,303}120$ and ^{289}Lv on the order of a few ms, and on the order of 10^{-2} s for ^{297}Og and 10^{-1} s for ^{299}Og. Maximum half-lives on the order of 10 s are predicted for ^{295}Lv, ^{283}Ds and ^{279}Hs, and on the order of 10^2 s is estimated for ^{291}Fl, ^{287}Cn and ^{273,275}Sg. The estimated branching ratio to low-lying excited states exceeds 55% for α-decay modes of ^{287,293}Lv, ^{297,299}Og and $^{295}120$, to ^{283}Fl($1/2^+$,72.9%), ^{289}Fl($3/2^+$), ^{293,295}Lv($1/2^+$) and ^{291}Og ($1/2^+$,56.5%). The estimated total T_α is less than the observed one in a few cases such as ^{281}Cn. Besides theoretical uncertainties, this may be attributed to the estimate incorporating all possible partial half-lives, whereas the experimental observation may capture only a subset of the allowed decay channels. We find that many of the estimated partial half-lives for ^{281}Cn are comparable to its observed half-life.

It should be noted that the predicted α-decay half-

lives and branching ratios are sensitive to the adopted Q_α values, as modest variations can lead to significant changes in the calculated decay properties, although the branching ratios between different decay modes of the same isotope are less affected. The dominant theoretical uncertainty originates from the underlying mass model and residual nuclear-structure effects, particularly in regions where competing configurations are close in energy. The Q_α values calculated here for the isotopes of unknown masses have typical uncertainties estimated at ±0.30–0.50 MeV. This theoretical uncertainty is estimated by considering the expected accuracy of the HFB-THO mass calculations, the response to reasonable changes in model inputs, and the additional approximations for odd-A and odd-odd systems, such as quasiparticle blocking and the choice of the blocked configuration, which may introduce a modest spread in the predicted masses and hence in Q_α. A sensitivity analysis within this range shows that absolute half-lives vary by roughly an order of magnitude, whereas branching ratios show only minor variations and the overall qualitative patterns are preserved. Thus, while the absolute numbers should be viewed with caution, the global systematics and relative patterns provide a reliable basis for comparison with future experimental data. The predicted α-decay branches and spin-parity assignments provide useful guidance for the future experimental identification of $Z=120$ isotopes. In practice, observed decays along their chains can be compared directly with the calculated sequences of parent and daughter states, while the proposed spin-parity assignments help resolve ambiguities among configurations that yield similar decay energies. The predicted fine-structure patterns, which include significant branches to excited daughter states, provide distinctive $\alpha-\gamma$ coincidence signatures that enable unambiguous parent assignment. The characteristic spin-parity sequences along each chain serve as a spectroscopic fingerprint distinguishing odd-neutron systems from their even-even counterparts. Moreover, the extended decay chains predicted here suggest that multiple correlated α decays may be observed, facilitating identification through recoil-α correlation techniques. The predicted branching patterns also reveal which decay channels are most probable for a given nucleus, aiding event assignment in recoil-decay measurements. Overall, these results offer testable signatures that can support future searches for $Z=120$ isotopes and improve the interpretation of limited experimental data.

IV. SUMMARY AND CONCLUSIONS

We conducted axially deformed, self-consistent HFB calculations for the proposed isotopes belonging to the even-odd $^{295-303}120$ decay chains to investigate their single-particle structure and partial decay modes. For both the structural calculations and the nucleus-nucleus potential used to determine half-lives within the PCM and WKB approximation, we employed the Skyrme-SLy4 EDF. We extracted ground-state configurations and deformations, low-lying excitations, and Q_α values for isotopes not yet observed or synthesized. With the GS being the lowest-energy blocked quasineutron configuration, excited states arise from blocking higher-energy quasineutrons, each of which determines a unique spin-parity. We determined α-decay partial half-lives and fine-structure patterns to the ground and excited states of the daughter nuclei.

The obtained evolution of single-neutron structure from $N=152$ to the $N=184$ shell closure is characterized by a systematic progression in both deformation and spin, beginning with the $1/2^+[620]$ and $3/2^+[622]$ states above the $N=152$ shell gap. With increasing N, the shape transitions to prolate deformation, where the $7/2^+[613]$ ($N=155-157$), $9/2^+[615]$ ($N=157$, $\beta_2\approx 0.26$), and $11/2^-[725]$($N=161$) orbitals alternate in dominance. The $3/2^+[611]$ orbital emerges as the GS at $N=163-167$ ($\beta_2=0.2-0.25$), shifting to higher energy as β_2 decreases ($N\geq 169$), and is followed by the $5/2^+[613]$, $9/2^+[604]$, and $1/2^+[611]$ states. A pivotal level rearrangement occurs within $N=169-171$ ($\beta_2=$ 0.12 – 0.21), where the $1/2^+[611]$ becomes the preferred GS, followed by $9/2^+[604]$, then $3/2^+[611]$ and $5/2^+[613]$. For $N=173(\beta_2=0.12-0.14)$, the $15/2^-[707]$ state becomes the next state after $1/2^+[611]$. Under relatively strong oblate deformation at $N=175$, the neutron occupation sequence is $1/2^+[640]$, followed by $3/2^+[642]$ and $5/2^+[642]$, then $1/2^+[600]$, while the $1/2^+[620]$ state becomes favored for weaker oblate deformations than $\beta_2=-0.12(N=175-177)$. For $\beta_2=$ –0.06 to –0.09, the $3/2^+[651]$ orbital is favored for $N=$ 177 and 179, alternating with the $1/2^+[651]$ state at $N=177$ and the $1/2^+[660]$ state at $N=179$. As N approaches 184, the nuclei become nearly spherical, and the lowest-energy orbitals are consistently the low-spin states $1/2^+[600]3d_{3/2^+}$, followed by $3/2^+[602]$, $3/2^+[611]$, and $1/2^+[631]$. The 19 low-lying neutron states in this region arise from the deformation of the spherical orbitals $2g_{7/2^+}$(one state), $3d_{5/2^+}(3)$, $1i_{11/2^+}(3)$, $2g_{9/2^+}(3)$, $1j_{15/2^-}(2)$, $2g_{7/2^+}(1)$, $4s_{1/2^+}(1)$, $1i_{13/2^+}(3)$ and $3d_{3/2^+}(2)$.

Rich decay schemes with more than five decay modes to low-lying states are obtained for ^{291}Og, ^{283}Fl, ^{281}Cn, and ^{275}Sg. We found that the decays of $^{295}120$, ^{291,297,299}Og, ^{271}Hs, ^{287,293}Lv, and ^{283}Fl proceed via excited states rather than directly to the GS. Even-odd isotopes exhibit longer decay chains than the corresponding even-even nuclei, with $^{301}120$ probably terminating at ^{277}Hs, while $^{295,297,299}120$ extending to Rf isotopes and $^{303}120$ expected to end at ^{279}Hs. Among the 22 isotopes that are either unsynthesized or lack observed α-decays, the predicted half-lives reach the millisecond range

(^{301,303}120, ^{289}Lv), fractions of a second (^{297,299}Og), tens of seconds (^{295}Lv, ^{283}Ds, ^{279}Hs), and hundreds of seconds for ^{291}Fl, ^{287}Cn, and ^{273,275}Sg. The branching ratio to low-lying excited states exceeds 55%, reaching 72.9%, for specific modes of ^{287,293}Lv, ^{297,299}Og, and ^{295}120. By providing detailed spectral estimates essential for isotope confirmation, these results establish a key spectroscopic baseline for guiding the search for new SHN.

References

[1] W. J. Swiatecki, Phys. Scr. **24**, 113 (1981)
[2] P. Ring, P. Schuck, *The Nuclear Many-Body Problem* (Berlin-Heidelberg: Springer, 2004).
[3] J. Dobaczewski, M. V. Stoitsov, W. Nazarewicz, Prog. Part. Nucl. Phys. **59**, 432 (2007)
[4] W. M. Seif, H. Anwer, A. R. Abdulghany, Ann. Phys. **401**, 149 (2019)
[5] S. A. Giuliani, Z. Matheson, W. Nazarewicz *et al*., Rev. Mod. Phys. **91**, 011001 (2019)
[6] G. Royer, J. Phys. G **26**, 1149 (2000)
[7] S. G. Nilsson, Dan. Mat. Fys. Medd. **29**, 16 (1955)
[8] S. Ćwiok, J. Dudek, W. Nazarewicz, Comput. Phys. Commun. **46**, 379 (1987)
[9] V. M. Strutinsky, Nucl. Phys. A **122**, 1 (1968)
[10] P. Möller, A. J. Sierk, Int. J. Mass Spectrom. **349**, 19 (2013)
[11] W. M. Seif, A. R. Abdulghany, A. Nasr, Int. J. Mod. Phys. E **31**, 2250074 (2022)
[12] N. Schunck, L. M. Robledo, Rep. Prog. Phys. **79**, 116301 (2016)
[13] M. Warda, L. M. Robledo, Phys. Rev. C **84**, 044608 (2011)
[14] G. D. Dracoulis, P. M. Walker, F. G. Kondev, Rep. Prog. Phys. **79**, 076301 (2016)
[15] W. M. Seif, A. R. Abdulghany, Phys. Rev. C **108**, 024308 (2023)
[16] W. M. Seif, A. Adel, N. V. Antonenko *et al*., Phys. Rev. C **107**, 044601 (2023)
[17] M. Asai, F. P. Heßberger, A. Lopez-Martens, Nucl. Phys. A **944**, 308 (2015)
[18] B. Birkenbach *et al*., Phys. Rev. C **92**, 044319 (2015)
[19] M. Ismail, W. M. Seif, W. M. Tawfik *et al*., Ann. Phys. **406**, 1 (2019)
[20] Y. Z. Wang, S. J. Wang, Z. Y. Hou, J. Z. Gu, Phys. Rev. C **92**, 064301 (2015)
[21] M. Ismail, W. M. Seif, W. M. Tawfik, Indian J. Phys. **96**, 1 (2022)
[22] W. M. Seif, A. R. Abdulghany, Phys. Rev. C **109**, 044326 (2024)
[23] J. P. Cui, Y. H. Gao, Y. Z. Wang *et al*., Nucl. Phys. A **1017**, 122341 (2022)
[24] J. H. Hamilton, S. Hofmann, Y. T. Oganessian, Annu. Rev. Nucl. Part. Sci. **63**, 383 (2013)
[25] Yu. Ts. Oganessian, V. K. Utyonkov, Nucl. Phys. A **944**, 62 (2015)
[26] M. Wang *et al*., Phys. Rev. C **106**, L051301 (2022)
[27] G. G. Adamian, L. A. Malov, N. V. Antonenko *et al*., Phys. Rev. C **97**, 034308 (2018)
[28] D. F. Rojas-Gamboa, N. G. Kelkar, O. L. Caballero, Phys. Rev. C **110**, 035804 (2024)
[29] K. Morita, Nucl. Phys. A **944**, 30 (2015)
[30] L. A. Malov, A. N. Bezbach, G. G. Adamian *et al*., Phys. Rev. C **106**, 034302 (2022)
[31] A. Nasr, W. M. Seif, A. R. Abdulghany, *et al*., Phys. Rev. C **113**, 024311 (2026)
[32] P. Marević, N. Schunck, E. M. Ney *et al*., Comput. Phys. Commun. **276**, 108367 (2022)
[33] R. N. Pérez, N. Schunck, R.-D. Lasseri *et al*., Comput. Phys. Commun. **220**, 363 (2017)
[34] M. V. Stoitsov, N. Schunck, M. Kortelainen *et al*., Comput. Phys. Commun. **184**, 1592 (2013)
[35] M. V. Stoitsov, J. Dobaczewski, W. Nazarewicz *et al*., Comput. Phys. Commun. **167**, 43 (2005)
[36] E. Chabanat, P. Bonche, P. Haensel *et al*., Nucl. Phys. A **635**, 231 (1998)
[37] S. S. Malik, R. K. Gupta, Phys. Rev. C **39**, 1992 (1989)
[38] W. M. Seif, J. Phys. G **40**, 105102 (2013)
[39] J. Dobaczewski, H. Flocard, J. Treiner, Nucl. Phys. A **422**, 103 (1984)
[40] M. Bender, P.-H. Heenen, P.-G. Reinhard, Rev. Mod. Phys. **75**, 121 (2003)
[41] E. Perlińska, S. G. Rohoziński, J. Dobaczewski *et al*., Phys. Rev. C **69**, 014316 (2004)
[42] D. Vautherin, D.M. Brink, Phys. Rev. C **5**, 626 (1972)
[43] J. W. Negele, D. Vautherin, Phys. Rev. C **5**, 1472 (1972)
[44] M. Chen, T. Li, J. Dobaczewski *et al*., Phys. Rev. C **103**, 034303 (2021)
[45] A. Nasr, W. M. Seif, A. R. Abdulghany, Chin. Phys. C **50**, 084110 (2026)
[46] Y. Z. Wang, Y. H. Gao, J. P. Cui *et al*., Commun. Theor. Phys. **72**, 025303 (2020)
[47] N. G. Kelkar, H. M. Castañeda, M. Nowakowski, Europhys. Lett. **85**, 20006 (2009)
[48] W. M. Seif, M. Ismail, A. I. Refaie *et al*., J. Phys. G **43**, 075101 (2016)
[49] W. M. Seif, M. M. Botros, A. I. Refaie, Phys. Rev. C **92**, 044302 (2015)
[50] G. R. Satchler, W. G. Love, Phys. Rep. **55**, 183 (1979)
[51] W. M. Seif, A. S. Hashem, J. Phys. G **47**, 085103 (2020)
[52] W. Zhang, Y. Gao, J. Cui *et al*., Phys. Rev. C **112**, 024319 (2025)
[53] J. Li, S. He, Y. Li *et al*., Phys. Rev. C **113**, 024330 (2026)
[54] Y. Z. Wang, F. Z. Xing, Y. Xiao *et al*., Chin. Phys. C **45**, 044111 (2021)
[55] W. M. Seif, A. Abdurrahman, Chin. Phys. C **42**, 014106 (2018)
[56] W. M. Seif, G. G. Adamian, N. V. Antonenko *et al*., J. Phys. G **52**, 015108 (2025)
[57] M. Wang, W. J. Huang, F. G. Kondev *et al*., Chin. Phys. C **45**, 030003 (2021)
[58] National Nuclear Data Center, Brookhaven National Laboratory, http://www.nndc.bnl.gov, retrieved November 2025
[59] F. G. Kondev, M. Wang, W. J. Huang *et al*., Chin. Phys. C **45**, 030001 (2021)
[60] W. M. Seif, A. R. Abdulghany, Eur. Phys. J. A **61**(11), 269 (2025)